Dielectric constants of amorphous hafnium aluminates: First-principles study

Hiroyoshi Momida,[1] Tomoyuki Hamada,[2,3] Yoshiteru Takagi,[3] Takenori Yamamoto,[4] Tsuyoshi Uda,[4] and Takahisa Ohno[1,3]
[1]*National Institute for Materials Science, 1-2-1 Sengen, Tsukuba, Ibaraki 305-0047, Japan*
[2]*Advanced Research Laboratory, Hitachi, Ltd., 1-280 Higashi-Koigakubo, Kokubunji, Tokyo 185-8601, Japan*
[3]*Institute of Industrial Science, University of Tokyo, 4-6-1 Komaba, Meguro, Tokyo 153-8505, Japan*
[4]*AdvanceSoft Corporation, 4-6-1 Komaba, Meguro, Tokyo 153-8904, Japan*
(Received 23 December 2006; revised manuscript received 28 February 2007; published 7 May 2007)

Amorphous model structures of hafnium aluminate having a Hf content of 0.2 (a-$Hf_{0.2}Al_{0.8}O_{1.6}$), alumina (a-Al_2O_3), and hafnia (a-HfO_2) are theoretically generated, and dielectric responses of the amorphous model structures are studied by the first-principles method. The models have corner, edge, and face shared AlO_n (n=4–6) and HfO_n (n=5–8) polyhedra, and the a-$Hf_{0.2}Al_{0.8}O_{1.6}$ model structures are phase separated at the atomistic level, having Al_2O_3 and HfO_2 domains. Calculated dielectric constants of the models increase with increasing Hf content, and the dielectric constant increase is dominated by the lattice polarization contribution to the dielectric constant. We found that low-frequency phonon modes having a frequency less than 200 cm^{-1} largely contribute to the high lattice dielectric constant and that inter-HfO_2 domain vibrations and vibration of atoms in distorted metal-oxygen polyhedra are dominant in the modes.

DOI: 10.1103/PhysRevB.75.195105 PACS number(s): 77.22.−d, 71.55.Jv, 61.43.Bn

I. INTRODUCTION

Recently, high-k materials (i.e., insulators having a higher dielectric constant than that of SiO_2 or SiON) have been investigated as the gate dielectrics of the next-generation complementary-metal-oxide-semiconductor (CMOS) transistor.[1–3] Amorphous alumina (a-Al_2O_3), hafnia (a-HfO_2), and hafnium aluminates (a-$Hf_xAl_{1-x}O_y$) are thought to be promising candidate high-k materials.

Amorphous high-k materials have several advantages over crystalline high-k materials as the gate dielectrics; i.e., the amorphous materials have an isotropic dielectric constant and no crystalline domain boundary, which generally works as the path of leakage current through the materials, and can be processed by the conventional CMOS fabrication process. The more important feature of amorphous high-k materials is that their dielectric and electric properties, thermal stability, and the material/Si-substrate interfacial structure can be changed by controlling their chemical composition and/or by doping of other element atoms (e.g., N atoms).[4–15]

Previous experimental studies have shown that the dielectric constants of a-$Hf_xAl_{1-x}O_y$ increase from the a-Al_2O_3 values (8–11) to the a-HfO_2 values (15–25) with increasing Hf content (x), while the crystallization temperature of a-$Hf_xAl_{1-x}O_y$ tends to decrease.[4–6] The crystallization temperature should be higher than the annealing temperature, typically about 1000 °C, during the CMOS fabrication process.[1] Therefore the a-$Hf_xAl_{1-x}O_y$ having a low x, e.g., 0.2–0.4, meets the requirements of the high-k gate dielectrics, showing better thermal stability than that of the a-HfO_2 and having a higher dielectric constant than that of the a-Al_2O_3.

In contrast to such experimental efforts, the structure and dielectric property of a-$Hf_xAl_{1-x}O_y$ have not yet been theoretically understood at the atomistic level because of difficulties in treating amorphous materials by theoretical calculation. Previously, we studied the dielectric response of the a-Al_2O_3 at the atomistic level by constructing a-Al_2O_3 model structures using classical molecular-dynamics (MD) calculations and by calculating static dielectric constants of the model structures by first principles.[16,17] We showed that the melt-and-quench MD calculation can generate a-Al_2O_3 model structures representing the experimental a-Al_2O_3 structure and that the dielectric response of a-Al_2O_3 can be studied by investigating the electronic as well as lattice dielectric constants of the model structures; the lattice dielectric constant was found to be dominant over the electronic one.

The aim of this study is to clarify structures and dielectric responses of a-$Hf_xAl_{1-x}O_y$ with $y=(3+x)/2$ [i.e., a-$(HfO_2)_x(AlO_{1.5})_{1-x}$ case] at the atomistic level, in a manner similar to that of our previous study. We theoretically generated model structures of a-HfO_2 and a-$Hf_{0.2}Al_{0.8}O_{1.6}$. Dielectric constants originating from electronic and lattice polarizations were calculated for these models by a first-principles method. We discuss dielectric responses of the a-$Hf_{0.2}Al_{0.8}O_{1.6}$ (x=0.2) models in comparison with those of the a-HfO_2 (x=1) models and a previously studied a-Al_2O_3 (x=0) model.

Calculated dielectric constants of the a-HfO_2 and a-$Hf_{0.2}Al_{0.8}O_{1.6}$ models are close to the corresponding experimental values, and the dielectric constant of the a-$Hf_{0.2}Al_{0.8}O_{1.6}$ models is in between those of the a-HfO_2 models and a-Al_2O_3 models. The results show that the dielectric constant of these amorphous models increases as the x increases, in accord with experiments. The increase is seen in both the electronic and lattice polarization contributions to the dielectric constant, and the increase in the lattice polarization contribution is more substantial. We found that the degree of the increase in lattice polarization differs between the a-$Hf_xAl_{1-x}O_y$ models and that the degree significantly depends on their structure. It was found that a-$Hf_{0.2}Al_{0.8}O_{1.6}$ models are phase separated at the atomistic level into HfO_2 and Al_2O_3 domains, and that their high dielectric constant is dominated by elastic vibrational modes, causing interdomain

vibrations and vibrations of atoms in distorted metal-oxygen polyhedra, with frequencies less than 200 cm^{-1}.

II. METHODS OF CALCULATIONS

Amorphous model structures of a-HfO_2 and a-$Hf_{0.2}Al_{0.8}O_{1.6}$ were generated by classical MD calculations under the *NPT* ensemble using a time step of 1.0 fs.[18–20] We used the empirical atom-atom pair potentials for metal oxides, which are parametrized by Matsui[21] and Yamasaki *et al.*[22] to reproduce experimental crystal structures and thermal properties of several metal oxides. The periodic boundary condition was used in the MD calculations, so that generated amorphous models have an unphysical translational periodicity. Previously, we examined the influence of such an unphysical translational periodicity on the dielectric constant of a-Al_2O_3 models by changing the unit-cell size.[17] The dielectric tensor of amorphous materials should be isotropic and diagonal, and we obtained reasonable dielectric tensors for the 120 atoms/cell models (a-$Al_{48}O_{72}$, subscripts denote number of atoms in a unit cell) while quite anisotropic dielectric tensors for the 60 atoms/cell models. The result indicates that the use of a unit cell with the number of atoms at least about 100 atoms/cell is necessary. Thus, the number of atoms in the unit cell of 96 and 104 atoms/cell were used for a-HfO_2 models (a-$Hf_{32}O_{64}$) and a-$Hf_{0.2}Al_{0.8}O_{1.6}$ models (a-$Hf_8Al_{32}O_{64}$), respectively.

The classical MD calculations were performed to obtain amorphous structures, using the melt-and-quench temperature control method as previously used for several oxides.[17,22–27] Molten states were equilibrated at a temperature (3000–3200 K) higher than the melting point of Al_2O_3 and that of HfO_2, and then the system temperature was cooled down to 300 K linearly with time using a constant cooling rate. Finally, the systems were maintained for 4.0 ps at 300 K and equilibrated. We obtained model structures using several cooling rates. During the melt-and-quench MD calculations, the length of the unit cell was allowed to change under the zero pressure condition, while the unit-cell vectors were fixed to the right angle.

Models used in this study were generated as follows. Two a-$Al_{48}O_{72}$ were obtained using the cooling rates of 0.54 K/fs (model A) and 0.27 K/fs (model B) for the initial structure of the α-Al_2O_3 crystal. Two a-$Hf_{32}O_{64}$ were generated using the cooling rates of 1.35 K/fs (model A) and 0.54 K/fs (model B) for the initial structure of the cubic hafnia (c-HfO_2) crystal. Three a-$Hf_8Al_{32}O_{64}$ models were calculated using the cooling rate of 0.54 K/fs, and their initial structures were the modified a-Al_2O_3 such that Al-O atoms were replaced by Hf-O atoms (models A, B, and C). The distributions of eight Hf atoms in the initial structures were as spatially homogeneous as possible. Note that the Hf atoms in the a-$Hf_8Al_{32}O_{64}$ tend to cluster during the calculations even for the initial structures, as will be discussed in Sec. III.

To obtain the realistic amorphous models, the cooling rate was a crucial parameter in the melt-and-quench simulations. In the case of a-SiO_2, effects of the cooling rates on the structure have been investigated in a wide range, and reliable models can be obtained by the slow cooling rates (such as 10^{13} K/s or slower).[28] Considering the a-SiO_2 case, it is necessary to choose a suitable range of the cooling rates also for the a-$Hf_xAl_{1-x}O_y$. For the slower cooling rates, however, the quenched structures of the a-$Hf_xAl_{1-x}O_y$ systems showed stronger tendency to crystallize, e.g., the radial distribution function had periodic discrete peaks, especially for smaller systems containing fewer number of atoms in a unit cell. Actually, the HfO_2 is known as a reluctant glass former, whereas the SiO_2 is a well-known glass former. Even for the a-Al_2O_3, very fast cooling rates are necessary to obtain amorphous states in experiments.[29] Thus we used relatively faster cooling rates (0.27–1.35 K/fs) to obtain the amorphous structures. The calculated structures were compared with the experimental results to confirm the reliability of the models, as will be discussed in Sec. III. In the case of a-Al_2O_3, the calculated structures were in the experimental range.[17] Note that the real films include vacancies, impurities, pores, nonstoichiometric composition, and so on. Their effects on the electrical and/or dielectric properties have been studied theoretically by using the crystals,[14,15] though our amorphous models do not include them. In addition, the real a-$Hf_xAl_{1-x}O_y$ have been prepared only in the thin-film states, usually by the deposition methods, and there is still a possibility that the films consist of microscopic crystals or phase-separated domains, as will be discussed in Sec. III.

Obtained final classical MD structures of the amorphous models were optimized by the first-principles method; the optimization was continued until all atomic forces became less than 1.0 mRy/bohr, keeping the unit cell of the models and thus the density. First-principles calculations are based on the density-functional theory (DFT) within the local-density approximation (LDA) using the plane-wave pseudopotential method.[30–34] We used a plane-wave cutoff energy of 25 Ry for the Kohn-Sham wave functions and a sampling **k** point of the Γ for the structure optimizations.

Dielectric constants (ε) were calculated as a sum of the electronic and lattice polarization contributions (electronic and lattice dielectric constants, ε^{ele} and ε^{lat}) based on first principles,[34]

$$\varepsilon = \varepsilon^{ele} + \varepsilon^{lat}. \tag{1}$$

The dielectric constant of the high-k materials could be quantitatively estimated by calculating these two contributions separately. Previous studies have shown that the high-k materials have large ε^{lat}.[2,3,15–17,35–40] Note that the orientational averages of dielectric tensors are discussed in this paper. The ε^{ele} was calculated by considering direct interband electronic transitions from valence to conduction bands in the Brillouin zone, as described in the time-dependent perturbation theory of optical properties calculation.[41,42] The imaginary part of ε^{ele} was calculated, and then the real part of ε^{ele} was obtained by the Kramers-Kronig relation. In this study, the ε^{ele} were calculated by using the sampling **k** points on the $2\times2\times2$ mesh and conduction bands up to about 50 eV above a valence-band top energy. The ε^{lat} is given as

$$\varepsilon^{lat} = \frac{4\pi e^2}{V}\sum_{\lambda}\left(\frac{Z_\lambda}{\omega_\lambda}\right)^2, \tag{2}$$

using phonon frequency ω_λ and mode effective charge Z_λ of a phonon mode λ. V is the volume of the unit cell. The ω_λ

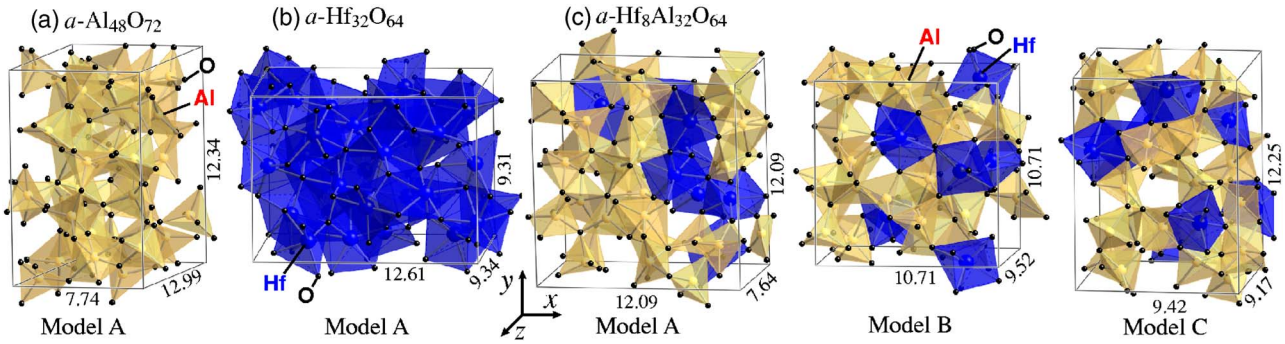

FIG. 1. (Color online) Amorphous model structures of (a) a-$Al_{48}O_{72}$ (model A), (b) a-$Hf_{32}O_{64}$ (model A), and (c) a-$Hf_8Al_{32}O_{64}$ (models A, B, and C). Dark and bright shaded polyhedra show HfO_n and AlO_n polyhedra, respectively (n is the coordination number). The unit cell is shown by line boxes, and O atoms outside the unit cell neighboring to Al or Hf atoms inside the cell also are shown. The length of the unit cell is shown in Å.

and the eigendisplacement vector $\xi_{\lambda i}$ of an atom i in a phonon mode λ at the zone center were calculated by diagonalizing dynamical matrices. The dynamical matrices were obtained as numerical first-order derivatives of the Hellmann-Feynman forces acting on atoms. The mode effective charge vector is given as

$$Z_{\lambda\alpha} = \sum_{i,\beta} Z^*_{i\alpha\beta}\xi_{\lambda i\beta}\frac{1}{\sqrt{M_i}}, \tag{3}$$

where α and β denote Cartesian indices, M_i is the mass of an atom i, and $Z^*_{i\alpha\beta}$ is the Born effective charge tensor of an atom i. The $Z^*_{i\alpha\beta}$ were calculated by the Berry phase polarization method.[43,44] The Z_λ is given as $Z^2_\lambda = 1/3(Z^2_{\lambda x}+Z^2_{\lambda y}+Z^2_{\lambda z})$.

III. MODEL STRUCTURES

Generated atomic structures of the amorphous models are shown in Fig. 1. Density, coordination number (CN) of Al and Hf, bond length distribution (BLD), and bond angle distribution (BAD) were analyzed for each amorphous model. CN of an Al atom of the amorphous models was defined as the number of O atoms around the Al atom, located within the Al atom centered sphere with a radius of 2.3 Å, and CN of a Hf atom of the models was defined similarly. The radius was determined from the first peak positions of Al-O and Hf-O BLDs of the models. The BLD was calculated in the same way as the radial distribution function (RDF), but BLD and BAD are calculated for first-principles optimized structures (not by taking the time average as usually done by MD calculation).

A. Amorphous Al_2O_3

Detailed results of the a-$Al_{48}O_{72}$ models have been reported previously in Ref. 17. CNs and densities are listed in Table I. In the a-$Al_{48}O_{72}$ models, four-coordinated Al atoms are predominant over five- and six-coordinated Al atoms; thus most of the Al atoms have smaller CN than Al atoms in α-Al_2O_3 crystal (CN=6). Calculated densities of the models are also smaller than values of α-Al_2O_3 crystal (4.0 g/cm^3). Experimental densities of 3.05–3.40 g/cm^3 and average Al CN of 4.1–4.8 have been reported for the a-Al_2O_3 films,[45–48] consistent with the calculated results.

Figure 2(a) shows the BLD of the a-$Al_{48}O_{72}$ (model A). At a long distance region over 4 Å, the total BLD of the model is flat and has a value of about 1, suggesting the absence of long-range structural order in the model structure. The total BLD of the model has a peak at 1.8 Å due to the Al-O bond, as shown by the partial BLD of the model. The total and partial BLDs show that the model has an amorphouslike structure, having a short-range order at the atomistic level. Partial BLD peaks of Al-Al and O-O are relatively broad, and the peak positions are at a longer bond distance than the Al-O BLD peaks. Calculated BLD peak positions are in good agreement with experimental RDF peak positions.[23,46–48]

Figure 2(b) shows the BAD of O-Al-O of the a-$Al_{48}O_{72}$ (model A). The total BAD of O-Al-O lies in a wide range and shows that these models have several O-Al-O angles, different from that of Al_2O_3 crystals, which have fixed discrete bond angles. To clarify the CN dependence of bond angles, CN-dependent partial BADs are calculated for O-Al-O in the model. The partial BADs for four-coordinated

TABLE I. Densities (ρ) and coordination number (CN) distributions of Al and Hf of calculated models.

		CN of Al (%)			CN of Hf (%)			
Model	ρ (g/cm^3)	4	5	6	5	6	7	8
			a-$Al_{48}O_{72}$					
A	3.27	60.4	29.2	10.4				
B	3.22	54.2	43.7	2.1				
			a-$Hf_8Al_{32}O_{64}$					
A	4.93	43.8	53.1	3.1	62.5	37.5	0	0
B	5.04	37.5	53.1	9.4	25.0	62.5	12.5	0
C	5.20	37.5	53.1	9.4	12.5	75.0	12.5	0
			a-$Hf_{32}O_{64}$					
A	10.20				6.2	59.4	31.3	3.1
B	10.61				9.4	56.2	34.4	0

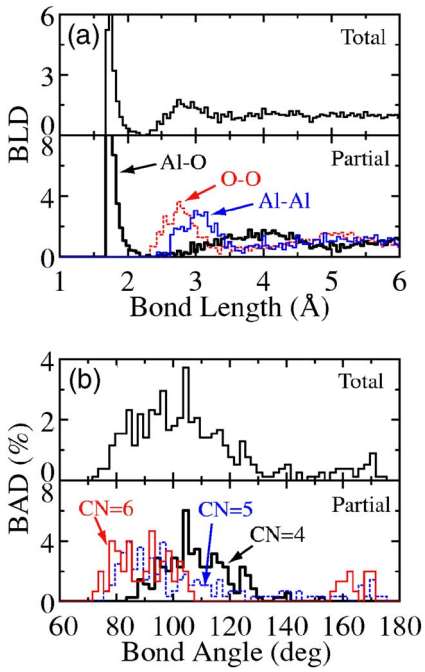

FIG. 2. (Color online) (a) Total and partial bond length distributions (BLDs) and (b) total and partial bond angle distributions (BADs) of O-Al-O in a-$Al_{48}O_{72}$ (model A).

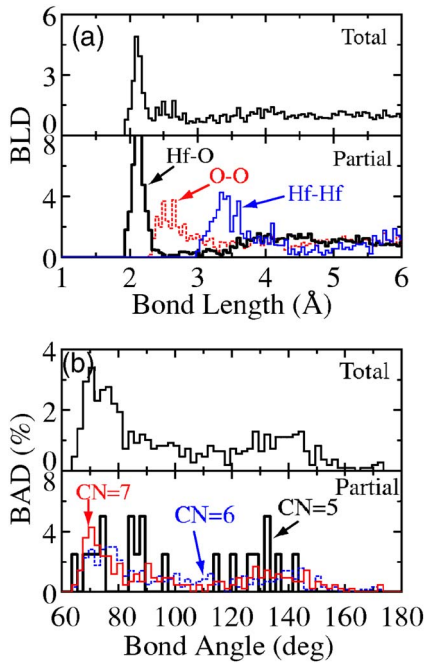

FIG. 3. (Color online) (a) Total and partial BLDs and (b) total and partial BADs of O-Hf-O in a-$Hf_{32}O_{64}$ (model A).

Al have a peak around 109.5°, which is the bond angle of the regular tetrahedral coordination, and those for six-coordinated Al have a peak around 90°, which is the angle of regular octahedral coordination. The total BAD of O-Al-O has the maximum at about 100°, and this accords with the model having four-coordinated Al atoms predominantly.

The above results indicated that the amorphous models are composed of the distorted AlO_n (n=4–6) polyhedra (n stands for the coordination number). The connectivity between the neighboring AlO_n polyhedra can be seen in Fig. 1(a). The structures have polyhedra connected, sharing one, two, or three O atoms; i.e., corner, edge, or face shared polyhedra. In the a-$Al_{48}O_{72}$ models, the corner-shared polyhedra type is dominant (about 85%), and the face-shared type is quite few (less than 1%), as reported by the classical MD calculation.[23] The smaller CN and the weak connectivity between polyhedra account for the amorphous models having a lower density than Al_2O_3 crystals.

B. Amorphous HfO_2

Calculated densities of the a-$Hf_{32}O_{64}$ models (Table I) are between experimental densities of monoclinic hafnia (m-HfO_2) and cubic hafnia (c-HfO_2), which are 10.1 and 10.9 g/cm^3, respectively. An experimental density of 9.68 g/cm^3 has been reported for thick a-HfO_2 films.[49] We could not obtain a-HfO_2 models having such a low density in the present study. It has been shown by positron annihilation experiments that actual a-$Hf_xAl_{1-x}O_y$ and a-$Hf_xSi_{1-x}O_y$ films have large open spaces in their amorphous structures.[50,51] Such large pore with a radius larger than 5 Å does not exist in our a-HfO_2 models, and this could be the reason for the difference between theoretical and experimental densities of a-HfO_2. Ikeda *et al.* reported that a-HfO_2 and a-$Hf_xSi_{1-x}O_y$ models with a large pore have been generated and investigated by the melt-and-quench first-principles MD simulations using the fixed unit cell during the MD simulations.[27]

Hf atoms in the a-$Hf_{32}O_{64}$ models are coordinated by five to eight O atoms, and six- and seven-coordinated Hf atoms are predominant (Table I). The m-HfO_2 and c-HfO_2 crystals have seven- and eight-coordinated Hf atoms, respectively. The result shows that most Hf atoms in the a-$Hf_{32}O_{64}$ models have a smaller coordination number than Hf atoms in the crystals, as shown by previous first-principles MD studies.[26,27]

Figure 3(a) shows BLD of the a-$Hf_{32}O_{64}$ (model A). The total and partial BLDs of a-$Hf_{32}O_{64}$ models show that the model has amorphouslike short- and long-range structural orders. The total BLD of the a-$Hf_{32}O_{64}$ model has a peak at 2.1 Å due to the Hf-O bond, as shown by the partial BLDs of the models. Partial BLD peaks of Hf-Hf and O-O are relatively broad, and the peak positions are at a longer bond distance than the Hf-O BLD peaks.

Figure 3(b) shows BAD of O-Hf-O for the a-$Hf_{32}O_{64}$ (model A). The total BAD of O-Hf-O for the model lies in a wide range and shows that these models have several O-Hf-O angles, different from that of HfO_2 crystals. CN-dependent partial BAD of O-Hf-O for the model shows that Hf atom having larger CNs has peak at smaller angles, as Al atoms in the a-Al_2O_3 model does [Fig. 2(b)]. The average CN of Hf atoms in the a-$Hf_{32}O_{64}$ models (CN=6.25–6.31) is larger than that of Al atoms in the a-$Al_{48}O_{72}$ models (CN =4.48–4.50). This explains why the BAD peak position of O-Hf-O for the a-$Hf_{32}O_{64}$ model is smaller in angle than that of O-Al-O for the a-$Al_{48}O_{72}$ model.

The amorphous models are composed of the distorted HfO_n (n=5–8) polyhedra (n stands for the coordination

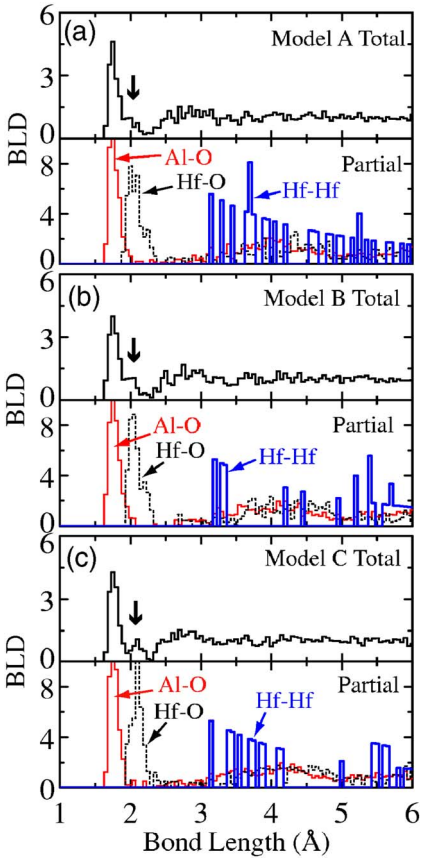

FIG. 4. (Color online) Total and partial BLDs of a-$Hf_8Al_{32}O_{64}$ models: (a) model A, (b) model B, and (c) model C. Shoulders at first peak of total BLD are shown by arrows.

number), and the connectivity between the neighboring HfO_n polyhedra can be seen in Fig. 1(b). The structures have polyhedra connected by sharing corner, edge, or face. In this view, the c-HfO_2 and m-HfO_2 crystals are composed of edge-shared HfO_8 polyhedra and corner- or edge-shared HfO_7 polyhedra, respectively. In the a-$Hf_{32}O_{64}$ models, the ratio of edge-shared polyhedra is also high (45% in model A and 41% in model B), relative to that of the a-$Al_{48}O_{72}$ models. In addition, there is an additional type of face-shared polyhedra (6% in model A and 9% in model B), which makes the system denser. The results account for the a-$Hf_{32}O_{64}$ models looking denser in structure compared with the a-$Al_{48}O_{72}$ models that are mainly composed of corner-shared polyhedra [Figs. 1(a) and 1(b)].

C. Amorphous $Hf_{0.2}Al_{0.8}O_{1.6}$

Calculated densities of the a-$Hf_8Al_{32}O_{64}$ models are in between those of a-$Al_{48}O_{72}$ and a-$Hf_{32}O_{64}$ models (Table I) and can approximately be given by the linear interpolation. To be precise, the a-$Hf_8Al_{32}O_{64}$ models are slightly denser by 4–12% than the interpolated values of 4.62–4.74 g/cm^3. Although experimental densities have not been reported in our knowledge, it has been shown that there are large open spaces in a-$Hf_{0.3}Al_{0.7}O_y$ films observed by positron annihilation experiments,[51] as already mentioned.

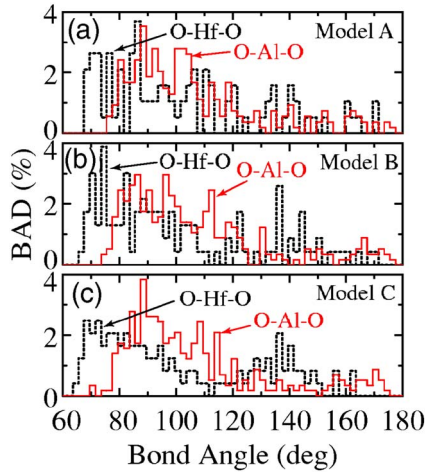

FIG. 5. (Color online) Total BADs of O-Al-O and O-Hf-O in a-$Hf_8Al_{32}O_{64}$ models: (a) model A, (b) model B, and (c) model C.

The a-$Hf_8Al_{32}O_{64}$ models have five- to seven-coordinated Hf atoms. The CN distribution of Hf atoms is strongly model dependent because the models have only eight Hf atoms in the unit cell but, in all the models, five- and/or six-coordinated Hf atoms are dominant. The predominant Hf CN of the a-$Hf_8Al_{32}O_{64}$ models is smaller than the Hf CN of the a-$Hf_{32}O_{64}$ and HfO_2 crystals. The CN of Al atoms in the a-$Hf_8Al_{32}O_{64}$ models is from 4 to 6, similar to that of a-$Al_{48}O_{72}$ models. The predominant CN of Al atoms is 4 and 5 in both the a-$Al_{48}O_{72}$ and a-$Hf_8Al_{32}O_{64}$ models, but average CN of Al atoms is larger for the a-$Hf_8Al_{32}O_{64}$ models (CN=4.59–4.72). CN of most Al atoms is smaller than 6, which is the Al CN of α-Al_2O_3 crystal.

Figures 4(a)–4(c) show total and partial BLDs of the a-$Hf_8Al_{32}O_{64}$ models A, B, and C, respectively. The partial Al-O and Hf-O BLD peak positions of the models are almost the same as the Al-O BLD peak position of the a-$Al_{48}O_{72}$ models and the Hf-O BLD position of a-$Hf_{32}O_{64}$ models, respectively, and this explains why the first peak of the a-$Hf_8Al_{32}O_{64}$ model total BLD has a shoulder at the dip (the shoulder is due to the Hf-O BLD peak). Partial BLD peaks of O-O, Al-Al, Hf-Al (not shown), and Hf-Hf are relatively broad in all models, and the peak positions are at a longer bond distance than the Al-O and Hf-O BLD peaks. Note that Hf-Hf BLD peak positions of the a-$Hf_8Al_{32}O_{64}$ models are more scattered compared with those of the a-$Hf_{32}O_{64}$ models. The scattered peak positions of the a-$Hf_8Al_{32}O_{64}$ models are due to the models having a smaller number of Hf atoms in their unit cell. Experimental RDF of Hf-based oxide films has been observed by the grazing incidence x-ray diffraction methods, and the RDF of a-$Hf_{0.3}Al_{0.7}O_y$ films shows an amorphous feature of the atomic structure.[52] The peak positions of 2.14 and 3.48 Å have been reported,[52] consistent with the calculated peak positions of Hf-O and Hf-Hf pair correlation, respectively.

Figures 5(a)–5(c) show total BADs of O-Al-O and O-Hf-O of the a-$Hf_8Al_{32}O_{64}$ models A, B, and C, respectively. The O-Al-O and O-Hf-O BADs are similar in distribution to the total O-Al-O BAD of the a-Al_2O_3 models and the total O-Hf-O BAD of the a-$Hf_{32}O_{64}$ models, respectively.

However, the O-Al-O BAD of the a-$Hf_8Al_{32}O_{64}$ models is slightly shifted toward the smaller angle, relative to that of the a-Al_2O_3 models, and the O-Hf-O BAD of the a-$Hf_8Al_{32}O_{64}$ models toward the larger angle, relative to that of the a-$Hf_{32}O_{64}$ models. The shift is due to the Al atom CN of the a-$Hf_8Al_{32}O_{64}$ models being higher in distribution than that of the a-Al_2O_3 models and the Hf atom CN of the a-$Hf_8Al_{32}O_{64}$ models being lower in distribution than that of the a-$Hf_{32}O_{64}$ models (Table I).

Detailed atomic structure of a-$Hf_xAl_{1-x}O_y$ films has not been clarified yet, but it is practically known that the films show a strong tendency for phase separation into Al_2O_3 and HfO_2 during the CMOS annealing (about 1000 °C) if x of the film becomes high.[4–7] Although the present study cannot discuss such phase separation at the mesoscopic level, calculated structures of the a-$Hf_8Al_{32}O_{64}$ models A, B, and C also have clustering Hf atoms connected by Hf-O-Hf bonds [Fig. 1(c)]. The a-$Hf_8Al_{32}O_{64}$ models have eight Hf atoms in a unit cell, and seven of the Hf atoms in model A are connected via the Hf-O-Hf bonds. Similarly, sets of four, two, and two Hf atoms are connected in model B, and sets of five and three Hf atoms cluster in model C. Model A (B) has the largest (smallest) size of Hf-O-Hf clusters, and this account for the difference in partial Hf-Hf BLD between the models at about 3–4.5 Å [Figs. 4(a) and 4(b)]. The results imply that a-$Hf_xAl_{1-x}O_y$ tend to phase separate in an atomic scale, even if their x is 0.2 and they look like homogeneous films in a mesoscopic scale. The clustering of the Hf atoms accounts for the observed Hf-Hf RDF high peak at 3.48 Å in the a-$Hf_{0.3}Al_{0.7}O_y$ film.[52] It has been reported that the x-ray diffraction spectra of the a-$Hf_xAl_{1-x}O_y$ films show crystalline HfO_2 peaks after the 1000 °C annealing even for $x=0.28$.[8] Note that the average CN of the Hf in the a-$Hf_8Al_{32}O_{64}$ models (CN=5.38–6.00) is much lower than that in the monoclinic (CN=7), cubic (CN=8), and orthorhombic crystal phases, and that all the Hf atoms also have the Hf-O-Al connections.

We used these model structures in an attempt to study dielectric responses of a-$Hf_xAl_{1-x}O_y$ with $x=0$, 0.2, and 1.

IV. RESULTS FOR DIELECTRIC CONSTANTS

A. Dielectric constant

Figure 6(a) shows calculated ε of several a-$Hf_xAl_{1-x}O_y$ models, a-$Al_{48}O_{72}$ models A and B ($x=0$) investigated in our previous study,[17] and those investigated in the present study: a-$Hf_8Al_{32}O_{64}$ models A, B, and C ($x=0.2$) and a-$Hf_{32}O_{64}$ models A and B ($x=1$). The values are listed in Table II.

Calculated ε increase with increasing x, and the trend is in accordance with experimental results.[4,6–9] The ε values for the a-$Al_{48}O_{72}$ and a-$Hf_{32}O_{64}$ models are in the reported experimental ranges of Al_2O_3 films[4,6,8,9,53,54] (8–11) and HfO_2 films (15–25),[4,6–9,12,13] respectively. Recently, Tomida *et al.* have studied the effects of structural phase transformations on the ε of HfO_2 films by doping small amount of Si atoms.[12] They show that the ε of HfO_2 films significantly depends on the film structures, and the observed ε are about 15 and 27 for the films crystallized to monoclinic and tetragonal (or cubiclike) phases, respectively, and about 20 for the amorphous films.[12] The experimental result shows good agreement with the present and reported ε values of the amorphous and the crystalline HfO_2,[15,26,38–40] as well as results for Al_2O_3.[17] Calculated ε of the a-$Hf_8Al_{32}O_{64}$ models are in between the a-$Al_{48}O_{72}$ and a-$Hf_{32}O_{64}$ values, and can be roughly estimated from these values by a linear interpolation. It has been experimentally reported that ε of $Hf_xAl_{1-x}O_y$ films increases almost linearly with increasing x in the range from 0 to about 0.5,[4,6,7,9] although the correlation between ε of $Hf_xSi_{1-x}O_y$ films and the x shows significant variety depending on the film preparation conditions.[13] Compared with the experimental values at a low x range,[4,6,7,9] calculated degrees of the increase of the ε from $x=0$ to $x=0.2$ are reasonable, though the calculated ε for these amorphous models differ even when the models have the same x.

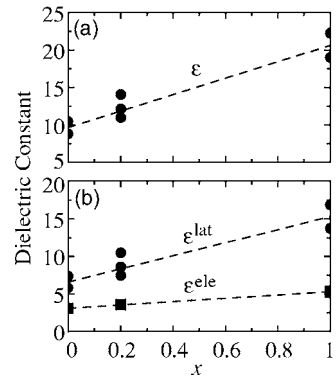

FIG. 6. (a) Dielectric constants (ε) and (b) electronic and lattice polarization contributions to the ε (ε^{ele} and ε^{lat}) of a-$Al_{48}O_{72}$, a-$Hf_8Al_{32}O_{64}$, and a-$Hf_{32}O_{64}$ models, which have Hf contents (x) of 0, 0.2, and 1, respectively. Broken lines are for linear interpolation.

Figure 6(b) shows calculated ε^{ele} and ε^{lat} against x. Both the ε^{ele} and ε^{lat} of the models increase with increasing x, and the increase of the ε^{lat} is more significant. The results show that the experimentally observed increase of ε of $Hf_xAl_{1-x}O_y$

TABLE II. Dielectric constants ($\varepsilon=\varepsilon^{ele}+\varepsilon^{lat}$) with electronic and lattice polarization contributions (ε^{ele} and ε^{lat}), and electronic band gap (E_g) of calculated models.

Model	ε	ε^{ele}	ε^{lat}	E_g (eV)
		a-$Al_{48}O_{72}$		
A	10.48	3.11	7.37	3.77
B	8.85	3.06	5.79	3.56
		a-$Hf_8Al_{32}O_{64}$		
A	12.14	3.55	8.59	3.57
B	11.01	3.55	7.46	3.01
C	14.07	3.61	10.46	2.93
		a-$Hf_{32}O_{64}$		
A	18.99	5.21	13.78	3.05
B	22.26	5.38	16.88	2.82

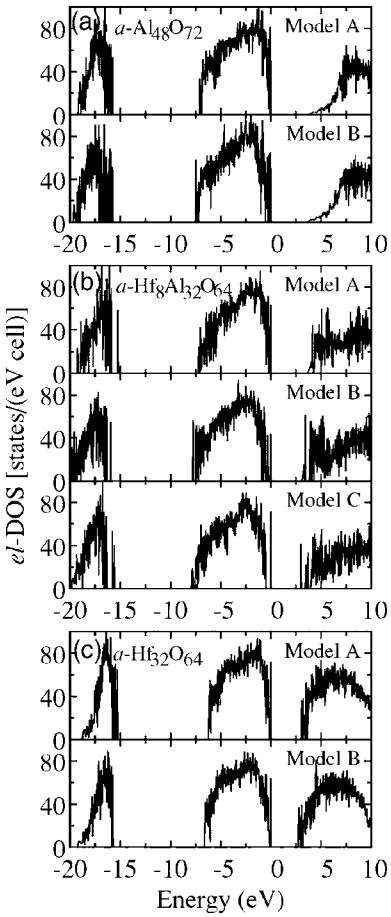

FIG. 7. Electronic density of states (*el*-DOS) of (a) a-$Al_{48}O_{72}$, (b) a-$Hf_8Al_{32}O_{64}$, and (c) a-$Hf_{32}O_{64}$ models. The top of the valence band is taken at the energy origin for each of the models.

with increasing x is mainly due to the increase of ε^{lat}. Zhao *et al.* have investigated structural and dielectric properties of a-ZrO_2 and a-HfO_2 by the first-principles method,[24–26] and ε^{lat} of 16.8 for a-HfO_2 has been reported,[26] consistent with the present results.

In the following, we analyzed the ε^{ele} and ε^{lat} of the amorphous models in relation to their electronic band and lattice vibration structures of the models, respectively.

B. Electronic dielectric constant

Figures 7(a)–7(c) show electronic density of states (*el*-DOS) of the a-$Al_{48}O_{72}$,[17] a-$Hf_8Al_{32}O_{64}$, and a-$Hf_{32}O_{64}$ models, respectively, calculated by using the $4\times4\times4$ **k** mesh. Valence bands of all the models in the energy range from −20 to −15 eV are mainly composed of s orbitals of O atoms and those in the range from −8 to 0 eV are of p orbitals of O atoms. All the models are insulators without midgap levels, contrary to Hf-based oxides with O vacancies.[14,15,56] On the other hand, conduction-band edge features of the models differ significantly, depending on whether the models have Hf atoms or not. Each of the a-$Al_{48}O_{72}$ models without Hf atoms has a low *el*-DOS at the band edge, while each of the a-$Hf_8Al_{32}O_{64}$ and a-$Hf_{32}O_{64}$ models with Hf atoms has a high *el*-DOS at the band edge. The differences are due to the fact that the conduction band edge states of the a-$Al_{48}O_{72}$ models are delocalized,[17] whereas those of the Hf-containing models have the Hf d orbital character and are localized. The *el*-DOS near the conduction-band edge becomes high with increasing x due to the localized Hf d characters.

Calculated electronic band gaps of the models are listed in Table II. Calculated band gaps of the a-$Al_{48}O_{72}$ and a-$Hf_{32}O_{64}$ models are smaller than experimental band gaps of a-Al_2O_3 films[10,11,55] (5–7 eV) and a-HfO_2 films (5–6 eV),[10,11,56] respectively. This is due to the DFT-LDA calculation, which usually underestimates experimental band gaps. Note that the experimental values depend on film structure, thickness, and other experimental conditions. It has been reported for a $Hf_xAl_{1-x}O_y$ film that the optical band gaps decrease linearly from Al_2O_3 (6.25 eV) to HfO_2 (5.56 eV) values with increasing HfO_2 mole fraction.[10] On the other hand, it has also been reported that the band gap decreases from Al_2O_3 (about 6.0 eV) to HfO_2 (5.6 eV) values with nonlinear dependence of the mole fraction by electron photoemission experiments, indicating less contribution of Hf at the conduction-band edge.[11] Within the DFT-LDA, calculated band gaps of the a-$Hf_{32}O_{64}$ models are also smaller than those of the a-$Al_{48}O_{72}$ models. Assuming that the underestimation is similar between the calculations, we expect that the band gap of $Hf_xAl_{1-x}O_y$ tends to be reduced with increasing x. Note that, to be precise, calculated band gaps of the a-$Hf_8Al_{32}O_{64}$ models depend on the lowest energy position of the localized Hf d state as seen in Fig. 7(b).

The above results indicate that electronic transitions from the valence O p bands to the conduction Hf d bands mainly contribute to the ε^{ele} of the models having Hf atoms. The increase of the ε^{ele} with increasing x could be attributed to these transitions, which have a lower transition energy. In fact, the imaginary part of the calculated dielectric function of each of the Hf-containing model has a higher peak due to the transitions from O p bands to the conduction-band edge at a lower energy.[57]

C. Lattice dielectric constant

Figure 8 shows average Born effective charges of Al, Hf, and O atoms of the a-$Al_{48}O_{72}$,[17] a-$Hf_8Al_{32}O_{64}$, and a-$Hf_{32}O_{64}$ models against x. The charges were obtained by taking the average of the Born effective charge tensors of atoms of each species and by calculating the third of the trace of the averaged tensor. The charges of the Hf and Al species increase in magnitude with increasing x, and the charge of O atoms linearly decreases in magnitude as x increases. The charges for each atomic species are similar between the models at the same x. To clarify the reason for the charge magnitude enhancement, we investigated correlations between the Born effective charge tensors of atoms and the atomic environment, and found that Al and O atoms in Al-O-Hf structures have the Born effective charges larger in magnitude than Al and O atoms in other Al-O-Al structures, respectively. The charge magnitude enhancement thus appears to be due to the increase of the number of the Al-O-Hf structures by Hf doping.

Figure 9 shows the calculated zone-center phonon density of states (*ph*-DOS) of the a-$Al_{48}O_{72}$ model A,[17]

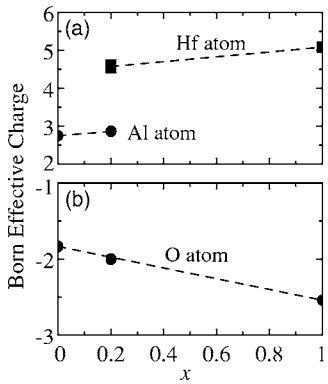

FIG. 8. Born effective charges of (a) Al and Hf, and (b) O atoms in a-$Al_{48}O_{72}$, a-$Hf_8Al_{32}O_{64}$, and a-$Hf_{32}O_{64}$ models, which have Hf contents (x) of 0, 0.2, and 1, respectively. The values are averaged over atoms in each atomic species and three diagonal components. The broken line in (b) is for linear interpolation.

a-$Hf_8Al_{32}O_{64}$ model A, and a-$Hf_{32}O_{64}$ model A. Total (upper panels) and partial (lower panels) *ph*-DOS are calculated as $\Sigma_\lambda \delta(\omega_\lambda - \omega)$ and $\Sigma_{i\in\tau,\lambda}|\xi_{\lambda i}|^2\delta(\omega_\lambda-\omega)$ for each atomic species τ, respectively.[24] The *ph*-DOS of the a-$Al_{48}O_{72}$ model distributes in a wide frequency range and is from both Al and O atom vibration state contributions. The *ph*-DOS of the a-$Hf_{32}O_{64}$ model distributes in a lower frequency range compared with that of the a-$Al_{48}O_{72}$. Vibration frequency distributions of Hf and O atoms in the a-$Hf_{32}O_{64}$ model are separated; the almost Hf atom vibration frequencies are lower and the almost O atom vibration frequencies are higher than about 300 cm^{-1}. The *ph*-DOS of the a-$Hf_8Al_{32}O_{64}$ model also distributes in a low-frequency range, and the low-frequency distribution less than 300 cm^{-1} is from Hf atom vibrations. These results indicate that the distribution of *ph*-DOS of a-$Hf_xAl_{1-x}O_y$ is lowered as the x is increased, and this lowering causes the enhancement of ε^{lat}.

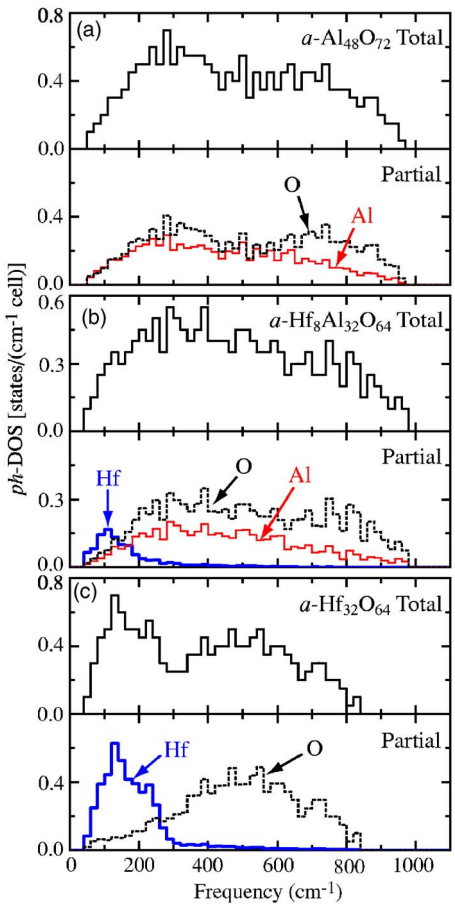

FIG. 9. (Color online) Histogram plots of zone-center phonon density of states (*ph*-DOS) of (a) a-$Al_{48}O_{72}$ (model A), (b) a-$Hf_8Al_{32}O_{64}$ (model A), and (c) a-$Hf_{32}O_{64}$ (model A). Histogram width is 20 cm^{-1}. Upper and lower panels show total and atom-decomposed *ph*-DOS, respectively.

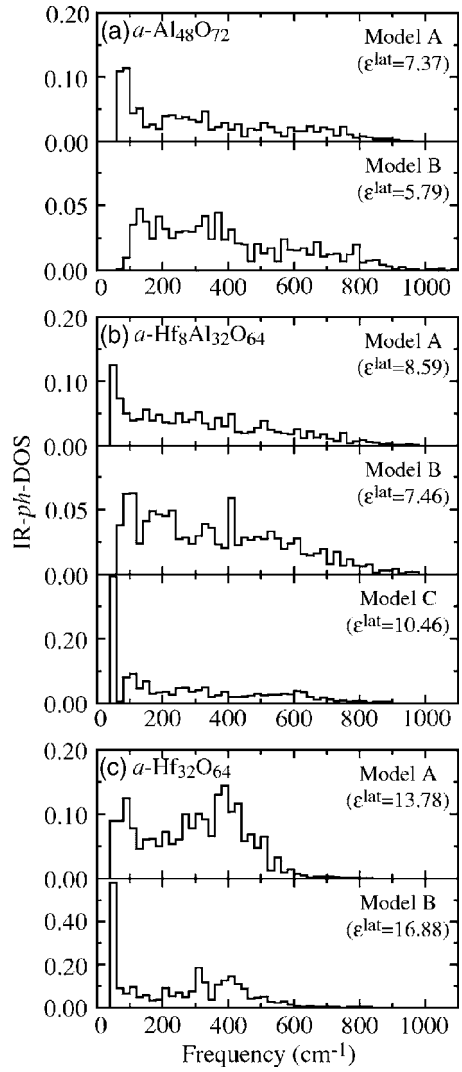

FIG. 10. Infrared active phonon density of states (IR-*ph*-DOS, see text) of (a) a-$Al_{48}O_{72}$, (b) a-$Hf_8Al_{32}O_{64}$, and (c) a-$Hf_{32}O_{64}$. Histogram width is 20 cm^{-1}.

To clarify phonon modes causing the ε^{lat} enhancement, infrared active *ph*-DOS (IR-*ph*-DOS), given as $(4\pi e^2/V)\Sigma_\lambda(3Z_\lambda^2/\omega_\lambda^2)\delta(\omega_\lambda-\omega)$,[24] were calculated. By the definition, the intensity of IR-*ph*-DOS is nonzero for infrared active modes, and the integration of IR-*ph*-DOS gives three times the lattice dielectric constant (sum of the diagonal components, $3\varepsilon^{lat}=\varepsilon_{xx}^{lat}+\varepsilon_{yy}^{lat}+\varepsilon_{zz}^{lat}$). Figure 10 shows IR-

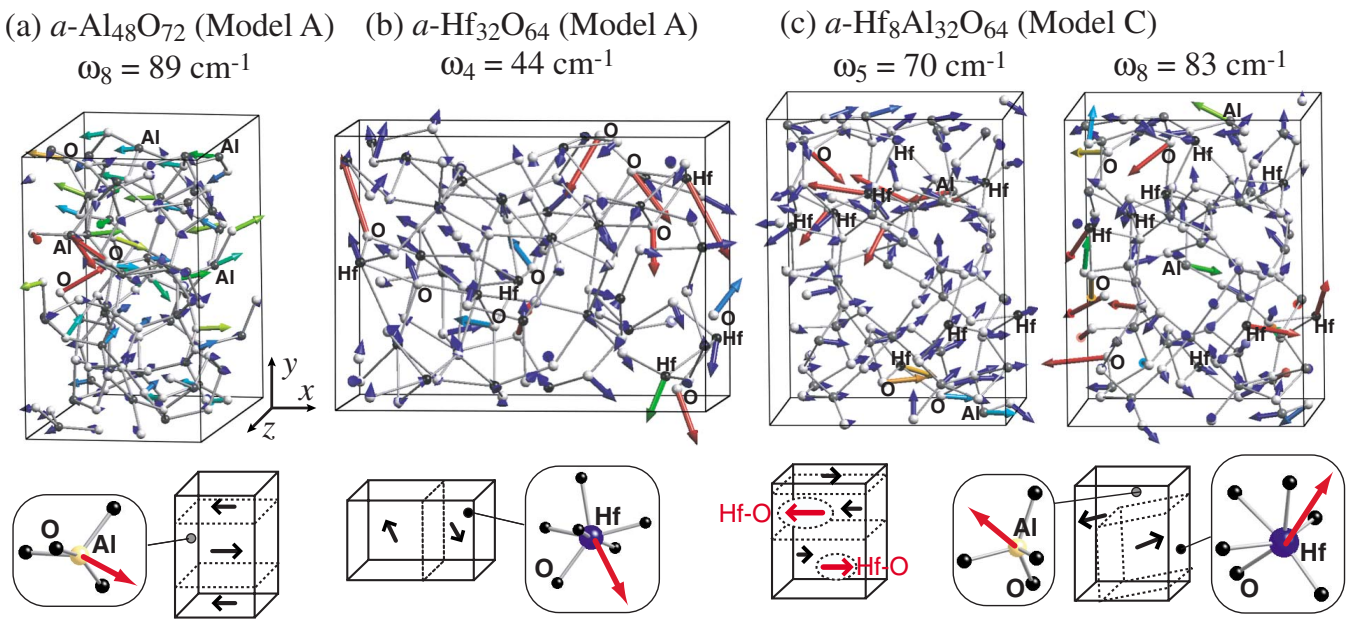

FIG. 11. (Color online) Examples of low-frequency phonon modes largely contributing to high lattice dielectric constant: (a) mode of a-$Al_{48}O_{72}$ (model A), (b) mode of a-$Hf_{32}O_{64}$ (model A), and (c) mode of a-$Hf_8Al_{32}O_{64}$ (model C). Arrows denote eigendisplacement vectors of the mode. Schematic pictures in lower part show rough sketches of the modes and polyhedra structures and positions of atoms largely vibrating in the modes.

ph-DOS of all the models of a-$Al_{48}O_{72}$, a-$Hf_8Al_{32}O_{64}$, and a-$Hf_{32}O_{64}$, along with $\varepsilon^{\mathrm{lat}}$ of the models. All the models have high peaks at frequencies less than 200 cm^{-1}, and the highest peak intensity of the models correlates with the $\varepsilon^{\mathrm{lat}}$ of the models. In the case of the a-$Hf_8Al_{32}O_{64}$ models, the intensity of low-frequency peaks significantly changes, depending on the models.

Atomic vibrations of the amorphous models at frequencies less than 200 cm^{-1} are analyzed to clarify atomic motions significantly contributing to $\varepsilon^{\mathrm{lat}}$ of the models. Figure 11 shows eigendisplacement vectors $\xi_{\lambda i}$ of phonon modes having high $(Z_\lambda/\omega_\lambda)^2$ values. Lattice vibrations of a solid are composed of elastic waves, and the low-frequency vibrations are composed of elastic waves having a long wavelength. Phonon modes shown in Fig. 11 are such modes. The a-$Al_{48}O_{72}$ and the a-$Hf_{32}O_{64}$ consist of hard domains, for example, which are mainly composed of edge- and face-shared polyhedra and are connected with each other by corner-shared polyhedra. The phonon modes of these models include the vibration of the domains [see Figs. 11(a) and 11(b)]. In the case of the a-$Hf_8Al_{32}O_{64}$ model, the phonon modes include distance stretching vibrations between HfO_2 domains [Fig. 11(c)]. Other low-frequency modes of the model include large displacements of atoms in some distorted AlO_n or HfO_n polyhedra. We previously found in the a-Al_2O_3 models that atoms in distorted polyhedra, such as polyhedra having planar structure, largely contribute to $\varepsilon^{\mathrm{lat}}$ via low-frequency modes.[17] Atoms in such planar polyhedra have weakly connected to neighboring atoms, and the potential around them is shallow in the direction perpendicular to the plane. Low-frequency modes of the a-$Hf_8Al_{32}O_{64}$ show that $\varepsilon^{\mathrm{lat}}$ of a-$Hf_xAl_{1-x}O_y$ is enhanced by elastic phonon modes as well as phonon modes localized at distorted polyhedra.

V. SUMMARY

We have calculated the atomistic and electronic structures of stoichiometric a-$Hf_xAl_{1-x}O_y$ $[y=(3+x)/2]$ models with the Hf content x of 0, 0.2, and 1, and investigated the dielectric response of the models, taking into account the electronic as well as lattice vibrational contributions to the response, by first principles. It was found that the models are phase separated to Al_2O_3 and HfO_2 domains at the atomistic level, and are insulators. Calculated dielectric constants were consistent with experimental results, and the dielectric constants increased with increasing x from 0 (the a-Al_2O_3 case) to 1 (the a-HfO_2 case). The lattice polarization contribution to dielectric constant was dominant over the electronic one, and low-frequency phonon modes with frequencies less than 200 cm^{-1} largely contribute to the large lattice polarization contribution. Inter-HfO_2 domain vibrations as well as vibrations of atoms in distorted AlO_n and HfO_n polyhedra significantly contribute to the higher lattice dielectric constant of the a-$Hf_xAl_{1-x}O_y$ models through these low-frequency phonon modes.

ACKNOWLEDGMENTS

The authors would like to thank Takahiro Yamasaki for valuable discussions. This research was supported by the RSS21 project and Grant-in-Aid for Scientific Research (No. 17064017) of MEXT of the Japanese Government. Computations were performed by using the supercomputer at the National Institute for Materials Science and Information Technology Center at the University of Tokyo.

[1] A. I. Kingon, J.-P. Maria, and S. K. Streiffer, Nature (London) **406**, 1032 (2000).
[2] G. D. Wilk, R. M. Wallace, and J. M. Anthony, J. Appl. Phys. **89**, 5243 (2001).
[3] J. Robertson, Eur. Phys. J.: Appl. Phys. **28**, 265 (2004).
[4] W. J. Zhu, T. Tamagawa, M. Gibson, T. Furukawa, and T. P. Ma, IEEE Electron Device Lett. **23**, 649 (2002).
[5] M.-Y. Ho, H. Gong, G. D. Wilk, B. W. Busch, M. L. Green, W. H. Lin, A. See, S. K. Lahiri, M. E. Loomans, P. I. Räisänen, and T. Gustafsson, Appl. Phys. Lett. **81**, 4218 (2002).
[6] G. D. Wilk, M. L. Green, M.-Y. Ho, B. W. Busch, T. W. Sorsch, F. P. Klemens, B. Brijs, R. B. van Dover, A. Kornblit, T. Gustafsson, E. Garfunkel, S. Hillenius, D. Monroe, P. Kalavade, and J. M. Hergenrother, in *2002 Symposium on VLSI Technology Digest of Technical Papers*, (IEEE Electron Device Society, Japan Soc. Appl. Phys., Honolulu, 2002), pp. 88–89.
[7] M. Koyama, Y. Kamimuta, M. Koike, M. Suzuki, and A. Nishiyama, in *Extended Abstracts of the 2003 International Conference on Solid State Devices and Materials (SSDM 2003)* (The Japan Society of Applied Physics, Tokyo, 2003), pp. 48–49; Y. Tamura, Y. Sugiyama, M. Yamaguchi, H. Minakata, Y. Tanida, T. Sakoda, M. Nakamura, and Y. Nara, *ibid.*, pp. 54 and 55.
[8] M. Koyama, Y. Kamimuta, M. Koike, M. Suzuki, and A. Nishiyama, Jpn. J. Appl. Phys., Part 1 **43**, 1788 (2004).
[9] M. Koyama, Y. Kamimuta, M. Koike, T. Ino, and A. Nishiyama, Jpn. J. Appl. Phys., Part 1 **44**, 2311 (2005).
[10] N. V. Nguyen, S. Sayan, I. Levin, J. R. Ehrstein, I. J. R. Baumvol, C. Driemeier, C. Krug, L. Wielunski, P. Y. Hung, and A. Diebold, J. Vac. Sci. Technol. A **23**, 1706 (2005).
[11] V. V. Afanas'ev, A. Stesmans, and W. Tsai, Appl. Phys. Lett. **82**, 245 (2003).
[12] K. Tomida, K. Kita, and A. Toriumi, Appl. Phys. Lett. **89**, 142902 (2006).
[13] H. Takeuchi and T.-J. King, Appl. Phys. Lett. **83**, 788 (2003).
[14] N. Umezawa, K. Shiraishi, T. Ohno, H. Watanabe, T. Chikyow, K. Torii, K. Yamabe, K. Yamada, H. Kitajima, and T. Arikado, Appl. Phys. Lett. **86**, 143507 (2005).
[15] H. Momida, T. Hamada, T. Yamamoto, T. Uda, N. Umezawa, T. Chikyow, K. Shiraishi, and T. Ohno, Appl. Phys. Lett. **88**, 112903 (2006).
[16] H. Momida, T. Yamamoto, T. Hamada, Y. Takagi, T. Uda, and T. Ohno, Trans. Mater. Res. Soc. Jpn. **30**, 889 (2005).
[17] H. Momida, T. Hamada, Y. Takagi, T. Yamamoto, T. Uda, and T. Ohno, Phys. Rev. B **73**, 054108 (2006).
[18] S. D. Bond, B. J. Leimkuhler, and B. B. Laird, J. Comput. Phys. **151**, 114 (1999).
[19] I. Souza and J. L. Martins, Phys. Rev. B **55**, 8733 (1997).
[20] E. Hernández, J. Chem. Phys. **115**, 10282 (2001).
[21] M. Matsui, Phys. Chem. Miner. **23**, 345 (1996).
[22] T. Yamasaki (private communication); C. Kaneta, Y. Kosaka, and T. Yamasaki, in *Semiconductor Technology (ISTC2002)*, Proceedings of the Second International Conference on Semiconductor Technology, edited by M. Yang (The Electrochemical Society, New Jersey, 2002), pp. 262–271.
[23] G. Gutiérrez and B. Johansson, Phys. Rev. B **65**, 104202 (2002).
[24] X. Zhao, D. Ceresoli, and D. Vanderbilt, Phys. Rev. B **71**, 085107 (2005).
[25] D. Vanderbilt, X. Zhao, and D. Ceresoli, Thin Solid Films **486**, 125 (2005).
[26] D. Ceresoli and D. Vanderbilt, Phys. Rev. B **74**, 125108 (2006).
[27] M. Ikeda, G. Kresse, T. Nabatame, and A. Toriumi, Mater. Sci. **23**, 401 (2005).
[28] K. Vollmayr, W. Kob, and K. Binder, Phys. Rev. B **54**, 15808 (1996).
[29] P. F. McMillan, Nature (London) **430**, 738 (2004); A. Rosenflanz, M. Frey, B. Endres, T. Anderson, E. Richards, and C. Schardt, *ibid.* **430**, 761 (2004); C. M. Jantzen, R. P. Krepski, and H. Herman, Mater. Res. Bull. **15**, 1313 (1980).
[30] P. Hohenberg and W. Kohn, Phys. Rev. **136**, B864 (1964).
[31] W. Kohn and L. J. Sham, Phys. Rev. **140**, A1133 (1965).
[32] D. Vanderbilt, Phys. Rev. B **41**, R7892 (1990).
[33] J. P. Perdew and Y. Wang, Phys. Rev. B **45**, 13244 (1992).
[34] CIAO, PHASE, and UVSOR, Institute of Industrial Science, University of Tokyo (http://www.fsis.iis.u-tokyo.ac.jp/en/).
[35] T. Yamamoto, H. Momida, T. Hamada, T. Uda, and T. Ohno, Thin Solid Films **486**, 136 (2005).
[36] G.-M. Rignanese, F. Detraux, X. Gonze, A. Bongiorno, and A. Pasquarello, Phys. Rev. Lett. **89**, 117601 (2002).
[37] S. A. Shevlin, A. Curioni, and W. Andreoni, Phys. Rev. Lett. **94**, 146401 (2005).
[38] G.-M. Rignanese, J. Phys.: Condens. Matter **17**, R357 (2005).
[39] X. Zhao and D. Vanderbilt, Phys. Rev. B **65**, 233106 (2002).
[40] G.-M. Rignanese, X. Gonze, G. Jun, K. Cho, and A. Pasquarello, Phys. Rev. B **69**, 184301 (2004).
[41] See, for example, G. Harbeke, in *Optical Properties of Solids*, edited by F. Abelès (North-Holland, Amsterdam, 1972), pp. 21–92; A. F. Starace, Phys. Rev. A **3**, 1242 (1971).
[42] H. Kageshima and K. Shiraishi, Phys. Rev. B **56**, 14985 (1997).
[43] R. D. King-Smith and D. Vanderbilt, Phys. Rev. B **47**, R1651 (1993).
[44] R. Resta, Rev. Mod. Phys. **66**, 899 (1994).
[45] S.-M. Lee, D. G. Cahill, and T. H. Allen, Phys. Rev. B **52**, 253 (1995).
[46] Y. Oka, T. Takahashi, K. Okada, and S. Iwai, J. Non-Cryst. Solids **30**, 349 (1979).
[47] R. Manaila, A. Dévényi, and E. Candet, Thin Solid Films **116**, 289 (1984).
[48] P. Lamparter and R. Kniep, Physica B **234-236**, 405 (1997).
[49] R. L. Puurunen, A. Delabie, S. V. Elshocht, M. Caymax, M. L. Green, B. Brijs, O. Richard, H. Bender, T. Conard, I. Hoflijk, W. Vandervorst, D. Hellin, D. Vanhaeren, C. Zhao, S. D. Gendt, and M. Heyns, Appl. Phys. Lett. **86**, 073116 (2005).
[50] A. Uedono, N. Hattori, A. Ogura, J. Kudo, S. Nishikawa, T. Ohdaira, R. Suzuki, and T. Mikado, Jpn. J. Appl. Phys., Part 1 **43**, 1254 (2004).
[51] A. Uedono, M. Goto, K. Higuchi, K. Shiraishi, K. Yamabe, H. Kitajima, R. Mitsuhashi, A. Horiuchi, K. Torii, T. Arikado, R. Suzuki, T. Ohdaira, and K. Yamada, Jpn. J. Appl. Phys., Part 1 **43**, 7848 (2004).
[52] I. Hirosawa, H. Kitajima, and K. Torii, Trans. Mater. Res. Soc. Jpn. **30**, 221 (2005).
[53] E. P. Gusev, E. Cartier, D. A. Buchanan, M. Gribelyuk, M. Copel, H. Okorn-Schmidt, and C. D'Emic, Microelectron. Eng. **59**, 341 (2001).
[54] K. S. Shamala, L. C. S. Murthy, and K. N. Rao, Mater. Sci. Eng., B **106**, 269 (2004).
[55] S. Miyazaki, J. Vac. Sci. Technol. B **19**, 2212 (2001).
[56] H. Takeuchi, D. Ha, and T.-J. King, J. Vac. Sci. Technol. A **22**, 1337 (2004).
[57] H. Momida, T. Hamada, and T. Ohno, Jpn. J. Appl. Phys. (to be published).